30. J. Chappellaz *et al.*, *J. Geophys. Res.* **102**, 15987 (1997).
31. S. Joussaume *et al.*, *Geophys. Res. Lett.* **26**, 859 (1999).
32. COHMAP Members, *Science* **241**, 1043 (1988).
33. F. E. Mayle, R. Burbridge, T. J. Killeen, *Science* **290**, 2291 (2000).
34. J. H. Yin, D. S. Battisti, *J. Clim.* **14**, 565 (2001).
35. S. Levitus, T. P. Boyer, *World Ocean Atlas 1994, Volume 4: Temperature*, NOAA Atlas NESDIS (U.S. Department of Commerce, Washington, DC, 1994).
36. P. M. Grootes, M. Stuiver, *J. Geophys. Res.* **102**, 26455 (1997).
37. D. Nürnberg, J. Bijma, C. Hemleben, *Geochim. Cosmochim. Acta* **60**, 803 (1996).
38. E. J. Brook, S. Harder, J. Severinghaus, E. J. Steig, C. M. Sucher, *Global Biogeochem. Cycles* **14**, 559 (2000).
39. T. Blunier, E. J. Brook, *Science* **291**, 109 (2001).
40. We thank P. deMenocal and A. van Geen for lab equipment and facilities; M. A. Cane, J. C. H. Chiang, and U. S. Ninnemann for helpful comments; M. Kienast for data; and J. Hayes at the National Ocean Sciences Accelerator Mass Spectrometry Facility for support with ^{14}C analyses. Supported by grants from NSF and a grants/cooperative agreement from the National Oceanic and Atmospheric Administration (NOAA). The views expressed herein are those of the authors and do not necessarily reflect the views of NOAA or any of its subagencies. Support for the curating facilities of the Lamont-Doherty Earth Observatory (LDEO) Deep-Sea Sample Repository is provided by NSF and the Office of Naval Research. Portions of this work were also supported by the LDEO Climate Center.

Supporting Online Material
www.sciencemag.org/cgi/content/full/297/5579/226/DC1
Materials and Methods
Tables S1 to S3

29 March 2002; accepted 30 May 2002

Two-Dimensional X-ray Waveguides and Point Sources

F. Pfeiffer,[1] C. David,[2] M. Burghammer,[3] C. Riekel,[3] T. Salditt[1]*

We show that resonant coupling of synchrotron beams into suitable nanostructures can be used for the generation of coherent x-ray point sources. A two-dimensionally confining x-ray waveguide structure has been fabricated by e-beam lithography. By shining a parallel undulator beam onto the structure, a discrete set of resonant modes can be excited in the dielectric cavity, depending on the two orthogonal coupling angles between the beam and the waveguide interfaces. The resonant excitation of the modes is evidenced from the characteristic set of coupling angles as well as the observed far-field pattern. The x-ray nanostructure may be used as coherent x-ray point sources with a beam cross section in the nanometer range.

X-ray scattering has had a tremendous impact as an experimental technique for studying the atomic structure of condensed matter. However, the technique is usually limited by two important constraints. First, it is characterized by two extremely opposed (separated) length scales: the microscopic x-ray wavelength $\lambda \cong 0.1$ nm and the macroscopic cross section D of the beam or, equivalently, the spot size on the sample. The sample therefore must be homogeneous over the entire length D, and the technique probes its ensemble-averaged structure. Second, the technique is restricted to static structural information owing to the elastic nature of the scattering events. X-ray scattering is insensitive to the dynamic nature of structural assemblies.

While synchrotron-based inelastic x-ray scattering and photon correlation spectroscopy address the second constraint, microbeam techniques challenge the first (*1*, *2*). If both constraints are to be circumvented simultaneously, small, intense, and fully coherent x-ray beams are needed. Micrometer-sized pinholes are currently used in photon correlation spectroscopy (*3*), but smaller coherent beams of $D \cong 10$ to 100 nm cannot be achieved by pinholes. Even if hypothetical pinholes of such size were available, the flux throughput would be insufficient. Spot sizes of ~90 nm have been obtained in the range of 5 to 8 keV by glass capillary optics (*1*), but these optics do not preserve coherence. Focused spot sizes of coherent beams can be achieved in the range of tens of nanometers for soft x-rays (*4*) by using diffractive lenses (Fresnel zone plates). However, because of the strong decrease of the absorption and phase shift with increasing photon energy, it becomes increasingly difficult to obtain small spot sizes at photon energies of 8 keV and above, and to our knowledge, no coherently focused spot sizes of less than several 100 nm have been reported to date (*5*).

X-ray waveguide structures present an approach for producing a coherent and divergent x-ray beam with precisely defined properties concerning shape and coherence (*6*), based on the principle of resonant beam coupling. The size of the beam at the exit of the waveguide is smaller than the thickness d of the waveguiding layer, which may reach down to $d \cong 10$ nm (*7*). The flux is efficiently increased by internal resonant field enhancement due to the generation of modes. Lensless projection phase contrast microscopy (*8*), as well as x-ray diffraction with submicrometer spatial resolution, has been demonstrated (*9*). The samples can be positioned outside the x-ray waveguide in the exiting beam or can be directly incorporated in the device. Macromolecular films (*10*) and colloidal suspensions (*11*) have already been investigated inside the resonantly enhanced field of a waveguide structure, making up its guiding layer.

To date, x-ray waveguide optics have been exclusively one-dimensional (1D), whereas most nanobeam applications would require two-dimensional (2D) point beams instead of 1D line beams. We present a proof of principle that the concept of resonant beam coupling can be generalized to two dimensions. To this end, we fabricated a rectangular x-ray waveguide by e-beam lithography, which compresses hard x-ray beams in two dimensions.

Visible light and infrared waveguides used in integrated optics are made of a rectangular dielectric core material, typically with an index of refraction in the range between 1.3 and 1.6, embedded in a dielectric cladding of a lower index to allow for guided mode propagation. The principal geometry of a rectangular waveguide is shown in Fig. 1, with width w and height h in the micrometer range. Contrarily, the index of refraction for hard x-rays $n = 1 - \delta + i\beta$ is always slightly smaller than 1, in proportion to the electron density of the material (*12*). The core material must therefore have a low electron density and yet also have a low absorption coefficient, and the cladding material with a comparably high electron density must provide a sufficiently high potential wall for the formation of guided modes. Apart from the optical constants, an important constraint is given by the condition that the chosen materials must be compatible with currently available lithography techniques to reach w and h values in the range of 100 nm and below. Considering these requirements, a combination of poly(methyl methacrylate) (PMMA) as a core material with a Cr cladding was chosen.

In order to analytically analyze the guiding characteristics of an x-ray waveguide and to optimize the design parameters, one has to solve the scalar wave equation

$$\nabla^2\Psi(x, z) + n^2(x, z)k^2\Psi(x, z) = 0 \quad (1)$$

for the electromagnetic field $\Psi(x, z)$, where $\nabla^2 = \partial^2/\partial x^2 + \partial^2/\partial z^2$, $k = 2\pi/\lambda$, and $n(x, z)$ is the profile of the refractive index given by the geometry of the guide (*13*). An exact

[1]Universität des Saarlandes, Im Stadtwald 38, Postfach 15 11 50, 66041 Saarbrücken, Germany. [2]Laboratory for Micro- and Nanotechnology, Paul Scherrer Institut, CH-5232 Villingen-PSI, Switzerland. [3]European Synchrotron Radiation Facility, Boite Postale 220, F-38043 Grenoble Cedex, France.

*To whom correspondence should be addressed. E-mail: salditt@mx.uni-saarland.de

analytical treatment of this problem is not possible, but approximate solutions by numerical methods are available in the literature of optical waveguides and can be made as accurate as desired (*14*). Using an approximate analytical approach (as specified below), we calculated the solutions of the mainly transverse electric (TE) guided modes in a rectangular dielectric PMMA/Cr waveguide with an index profile given by the following (*15*, *16*): $n(x, z) = n_1$ for $|z| \leq h/2$ and $|x| \leq w/2$, and $n(x, z) = n_2$ for $|z| > h/2$ and $|x| > w/2$. The calculations have been carried out for different values of w, h, n_1, n_2, and λ, with the results shown for parameter values corresponding to the experiment discussed below (Fig. 2A) (*17*, *18*).

The solution of Eq. 1 for the given geometry is a set of propagation modes with electric field-distributions of alternatively sine and cosine shape in the x and z directions, propagating along the y axis with a wave vector k_y^{intern} (*19*). The wave function $|\Psi^{pq}(x, z)|^2$ in the core (and the cladding) can be parameterized by the resonance orders with respect to the x and z directions. For each resonance, a pair of two internal angles, ϕ_{intern} (in the x direction) and α_{intern} (in the z direction), can be attributed, corresponding to a classical ray optics approach (*20*). The overall number of supported modes is then given by the restriction that α_{intern} and ϕ_{intern} must be smaller then the internal critical angle, because no total internal reflection and thus no mode propagation is possible for higher internal propagation angles (*21*, *22*).

The angular position of mode excitation in the guide as a function of the two internal angles, ϕ_{intern} and α_{intern}, can be illustrated in a 2D plot (Fig. 2B). Mode excitation is indicated by a black dot with the corresponding order in ϕ_{intern} and α_{intern} space. For comparison with the experimental values below, the calculated values of ϕ_{intern} and α_{intern} are displayed in table S1. The fundamental Ψ^{11} mode, for example, corresponds to a pair of angles, $\phi_{intern}^{11} = 0.0186°$ and $\alpha_{intern}^{11} = 0.0391°$, and to a cosine-shaped field distribution with its maximum in the waveguide center (*23*).

In the case of visible light, where laser spot sizes are on the order of the waveguide cross section, efficient excitation of guided modes is usually achieved by directing the beam onto the front face of the guide. For x-rays, however, the incoming beam size is much larger than the lateral dimensions of the waveguide cavity; normal incidence on the waveguide front would inevitably lead to a huge loss of intensity. A solution to this coupling problem is given by the resonant beam coupling mechanism, which has been successfully introduced for planar x-ray waveguides (*6*). The basic idea is to illuminate the whole structure by a wide beam (on the order of 20 to 200 μm) and to achieve coupling under resonance condition through a thin cladding layer at the top side of the guide, rather than its front face. At the end of the structure, photons trapped in the core of the guide (or guiding layer) exit the waveguide (*24*), leading to a coherent and divergent beam with well-defined properties of shape, phase, and divergence, directly related to the wave field inside the device. The 2D shape of the far-field pattern $I^{pq}(\phi_f, \alpha_f)$ of the Ψ^{pq} mode can be calculated from the complex wave field inside the rectangular guide by application of the Huygens principle and Fraunhofer diffraction, yielding

$$I^{pq}(\phi_f,\alpha_f) = I_0 \left| \int_{-\infty}^{+\infty}\int_{-\infty}^{+\infty} \Psi^{pq}(x, z) \times e^{ik(\sin(\phi_f)x + \sin(\alpha_f)z)}\, dxdz \right|^2 \quad (2)$$

To experimentally demonstrate resonant mode propagation in 2D x-ray waveguides, we fabricated a series of differently designed waveguides (Fig. 1); 480-μm-thick Si(111) wafers were used, coated with a 71.4-nm Cr layer by electron beam evaporation. Next, a PMMA layer of h = 62.2 nm was deposited by spin-coating. The waveguiding core was then defined as a stripe of PMMA with a width ranging between $w \cong$ 50 and 300 nm, using an electron beam lithography system and subsequent reactive ion etching. Finally, the Cr cladding for the top and the side interfaces was deposited under an angle of ±45° to cover the core with a uniformly thick and smooth cladding layer of 6.1 nm. This relatively small thickness of the Cr cladding was chosen to both allow for efficient beam coupling through the cladding layer and at the same time provide enough optical confinement. An undulator x-ray beam of wavelength λ = 0.097 nm was used in a setup described in (*25*, *26*).

To experimentally determine the geometric parameters of the fabricated devices, as well as the layer densities essential for the optical properties, we carried out two types of reflectivity measurements. First, standard reflectivity curves on the unstructured Si/Cr/PMMA/Cr film in the yz plane were measured and analyzed to determine the height of the guiding layer, the thickness of the cladding on top, and their densities (Fig. 3B, top curve) (*27*). Second, a nonconventional reflectivity scheme was applied to measure lateral structures of the waveguide stripe in the xy plane (varying $\phi_i = \phi_f$ at constant $\alpha_i = \alpha_f$), revealing the stripe width w and the thickness of the cladding at the side walls (*28*) (Fig. 3A, top curve). At the same time, the bottom curves of Fig. 3, A and B, show the intensity measured at $\phi_f = 0$ and $\alpha_f = 0$, as a function of ϕ_i and α_i, respectively. As known from 1D waveguides, the cusps in the reflectivity curves (Fig. 3, A and B, top curves) and the sharply enhanced signal in the forward direction [so-called 1:1 scans (Fig. 3, A and B, square symbols)] correspond to the resonance angles, where guiding modes lead to emission of photons at the device exit. The solid lines in the top curves (reflectivities) of Fig. 3, A and B, are least squares fits by the Parratt algorithm (*29*). The modes in the bottom curves [1:1 scans (square symbols)] of Fig. 3, A and B, were analyzed by multi-Gauss functions (solid lines). The center positions of the peaks are the mode angles displayed in the last column of table S1.

Although these data already give a strong indication of the 2D nature of the resonances, it is important to probe the excitation characteristics as a function of both incidence angles ϕ_i and α_i. To this end, we scanned ϕ_i and α_i in the form of a 2D mapping with the detector directed along the optical axis of the guide, at $\phi_f = \alpha_i = 0$. The detector slits were adjusted to integrate over ±0.01° in ϕ_f and

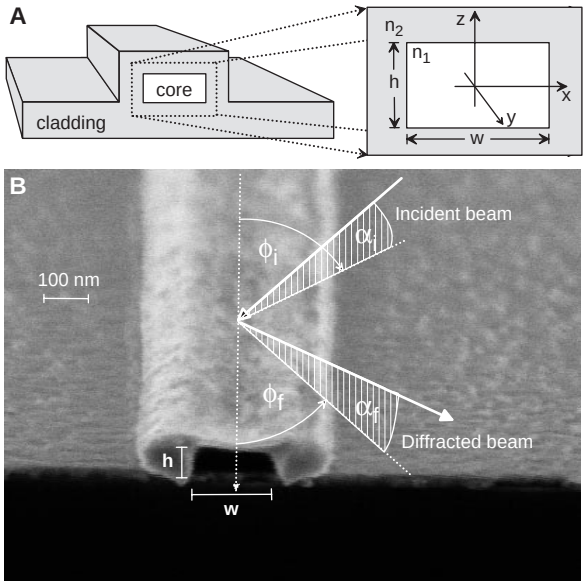

Fig. 1. (**A**) Sketch of a dielectric x-ray waveguide nanostructure (core width w and core height h) of refractive index n_1 embedded in the cladding layer of refractive index n_2. (**B**) Scanning electron microscope image of a waveguide nanostructure on a Si wafer, with the PMMA core (dark) and the Cr cladding (light).

$\pm 0.02°$ in α_f. Pronounced maxima were observed in the expected range of angles, indicating the excitation of modes. In contrast to the calculation of Fig. 2B, the fundamental Ψ^{11} mode was not observed at ($\phi_i = 0.0186°$, $\alpha_i = 0.0391°$), but at ($\phi_i = 0.019°$, $\alpha_i = 0.109°$) (see table S1). This effect is due to the particular mechanism of coupling the incoming beam into the waveguide structure. According to Snell's law, the beam is refracted when crossing the horizontal *xy* interfaces (top air/Cr and PMMA/Cr interfaces), so that the experimentally observed "external" coupling angles α_i and ϕ_i are shifted with respect to the "internal" mode angles α_{intern} and ϕ_{intern}. Consequently, the modes should occur at the positions marked in Fig. 2C rather than at those marked in Fig. 2B.

As can be seen in table S1, all modes exhibit a (vertical) shift that is in quantitative agreement with refraction at the horizontal interfaces, according to $\alpha_{intern} = (\alpha_i^2 - \alpha_{c,core}^2)^{1/2}$. However, refraction in the horizontal direction is not observed. Thus, we must assume an almost perfect matching between the external angle ϕ_i and the internal mode-excitation angle ϕ_{intern} in the *x* direction, and there is a significant shift due to refraction in α_i and α_{intern} (*z* direction). However, the measured intensities of the α_i and ϕ_i mapping in Fig. 2E still do not coincide with the refraction-corrected values of Fig. 2C. Rather than a rectangular array, the mode angles occur as a pattern composed of discrete circular segments or streaks at constant values of $k_{xz}^2 = k_{x,intern}^2 + k_{z,intern}^2$ (*19*). This observation suggests a smearing or mode coupling between different modes of constant radial wave vector, which can quantitatively be taken into account by a Gaussian broadening in the variable k_{xz} (Fig. 2D) (*30*).

Two conclusions can be drawn from these observations: (i) The beam couples into the waveguide structure mainly through the top surface. This seems reasonable, as the waveguide structure has a rather large width *w* and a small height *h*. This geometry likely favors coupling through the top surface, rather than through the side walls. An additional asymmetry of the vertical and horizontal interfaces of the waveguide is given by the presence of the substrate and the associated standing wave field building up at grazing angles. (ii) There is a partial coupling of modes characterized by a constant internal radial wave vector, possibly induced by rounded edges and other imperfections. In fact, the shape of the guide cannot be assumed to be perfectly rectangular. In the limiting case of a cylindrical cavity (e.g., polymer fiber coated by metal), full radial symmetry would be expected in the mapping. Finally, the resonances must indeed be of 2D nature, because the excitation in Fig. 2E is not equivalent to that of a conventional planar guide. The particular coupling mechanism that we suggest here is supported by quantitative comparison between the calculated and observed mode angles in table S1, which agree within the angular positioning accuracy of the instrument.

In view of possible fabrication errors, particularly with regard to interfacial roughness, it may seem surprising that resonant modes of 0.1-nm radiation can be excited in an imperfect device. However, it is important to note that the root-mean-square (rms) roughness σ enters the x-ray optical formulas only in form of the so-called Névot-Croce factor (Rayleigh criterion in visible light optics), that is, as $\exp(-k_{xz}k_{xz,intern}\sigma^2/2)$. Accordingly, the small values of the incidence angles efficiently prevent the damping effect of σ (*31*).

To determine the Fraunhofer diffraction pattern of an excited mode and to quantitatively compare it to the prediction according to Eq. 2, we measured the intensity distribution as a function of ϕ_f and α_f, using a 2D charge-coupled device (Fig. 4). The far-field intensity pattern of the fundamental Ψ^{11} mode (excited at $\phi_i = 0.019°$ and $\alpha_i = 0.109°$) is shown as a function of ϕ_f and α_f, after correction for detector sensitivity and background. The 2D image and, particularly, the integrated 1D cross sections in the ϕ_f and α_f directions exhibit the expected Gaussian shape. We conclude that the beam exiting from the waveguide has divergences of 0.052° and 0.084° [full width at half maximum (FWHM)] in the ϕ_f and α_f directions, respectively. The exit beam divergence was quantitatively confirmed by measurements of the beam cross section (not shown here) using a pinhole mounted on a piezo *xyz* stage at a distance of ≅1.0 mm behind the waveguide (*32*). The total output flux of the lowest excitation order was 2.0×10^4 photons/s (*33*).

The far-field simulation according to Eq. 2, and corresponding to the geometric parameters derived from the fits in Fig. 3, is plotted in Fig. 4, along with the measured cross sections, showing almost perfect agreement. Because the only fitting parameter in the simulation is the maximum intensity I_0, which does not affect the shape of the modes, we conclude that the beam emerging from the waveguide has the shape expected for the

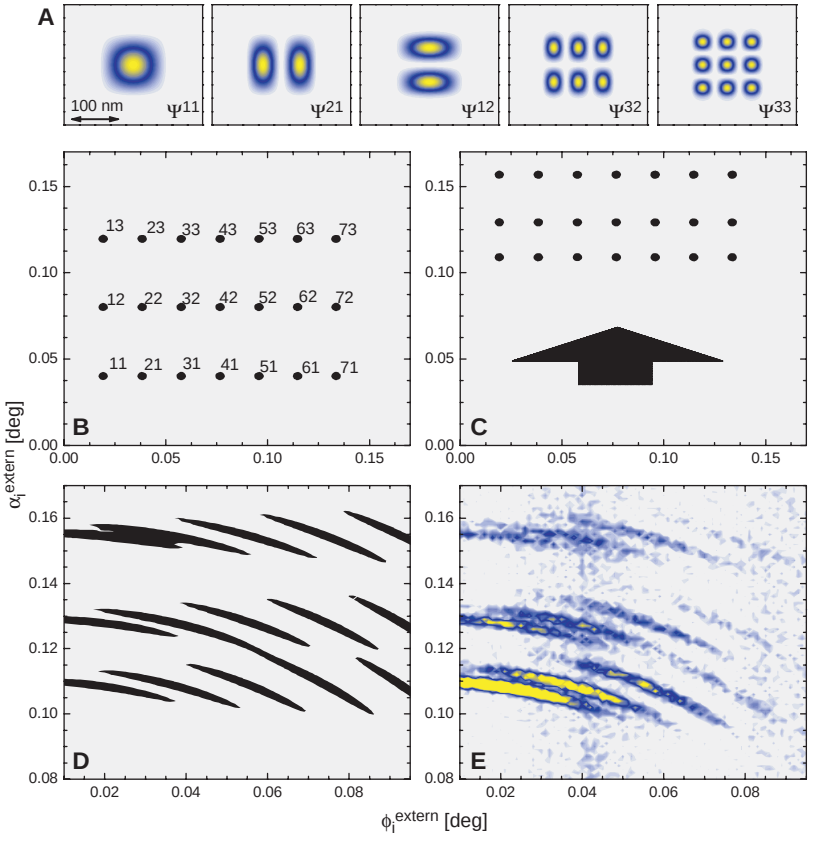

Fig. 2. (**A**) Simulation of the field intensity distribution in the waveguide core for the parameters of the experimental nanostructure, parameterized by the 2D excitation order. Simulated excitation characteristics of modes as a function of the external coupling angles (ϕ_i^{extern}, α_i^{extern}) assuming (**B**) no refraction, (**C**) refraction in the vertical plane of incidence, and (**D**) refraction and smearing along a constant radial wave vector in the guide. (**E**) Measured excitation pattern as a function of (ϕ_i^{extern}, α_i^{extern}) with the detector placed in the direction of the *y* axis to collect the photons diffracted at the exit of the guide. The similarity of the observed and simulated excitation characteristics in (D) indicates the generation of 2D resonances.

Ψ^{11} resonance mode. This means that the x-ray beam has a cross section of 68.7 nm by 33.0 nm at the exit of the nanostructure, which is, to our knowledge, the smallest spot size for hard x-rays ever achieved.

Although we were able to experimentally determine the angular position in ϕ_i and α_i for many higher order mode excitations (by integrating over a big part of the far-field pattern), a detailed measurement of the corresponding far-field pattern has yet not been possible with the current setup. This was mainly due to the fact that higher order modes are associated with maxima spaced farther away from the optical axis of the guide and thus closer to the tails of the primary and specularly reflected beams.

Thus, we experimentally demonstrated that these devices can be used for the production of a coherent x-ray point source with a beam cross section in the nanometer range. This proof of principle relies on three main pieces of evidence, which all underline the 2D nature of mode excitation and propagation: (i) the excitation characteristics of the 2D waveguide structure as discussed above and presented in Fig. 2, (ii) the cusps in the reflectivity measured in the vertical and horizontal directions as shown in Fig. 3, and (iii) the Fraunhofer far-field diffraction pattern displayed in Fig. 4, which exhibits the expected divergence both in the horizontal and vertical directions. We stress that the x-ray nanostructure discussed here is a simple optical device, filtering out an extended but parallel synchrotron beam (plane wave) incident on the sample and transforming it to a divergent but initially quasi–point-like beam at the exit of the guide. The exiting beam is fully coherent owing to the fact that only the plane wave component of the incident beam fulfills the coupling condition. Therefore, the device acts as a coherence filter.

The perspective of a powerful x-ray point source is only realistic if the coupling efficiency can be considerably increased over the values estimated here in this proof of principle (*33*). To this end, it can be expected that devices with much higher perfection (interfacial roughness, figure error, and homogeneity of guiding medium and cladding) can be developed. Further progress may derive from improved material compositions or adapted prefocusing optics. Moreover, 2D x-ray waveguides are not limited to the relatively simple geometry presented here. X-ray nanostructures can be conceived, in which the beam is first coupled into a guiding layer as in the conventional 1D case and then into a stripe or channel geometry (fig. S1), rather than directly into a 2D confinement (optical cavity).

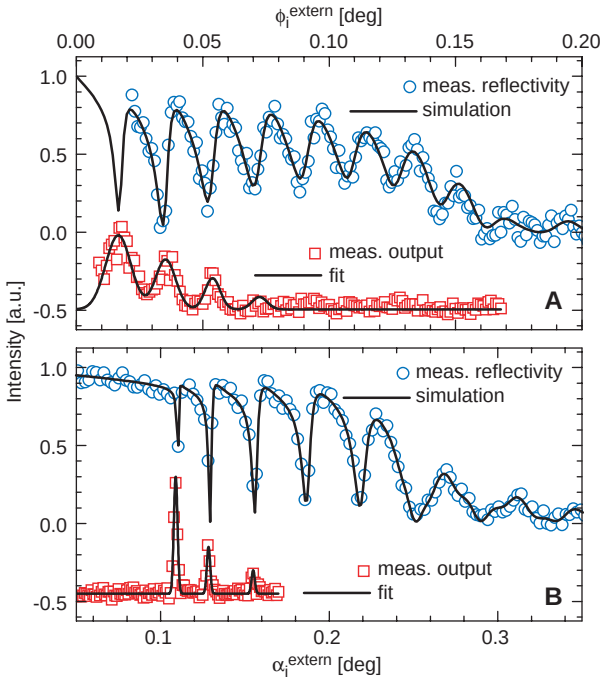

Fig. 3. (**A**) Measured (open circles) and simulated intensity (solid line) reflected in the horizontal direction at $\phi_i = \phi_f$ as a function of ϕ_i and at constant $\alpha_i = 0.109°$ (first-order excitation in the *z* direction). The bottom curve (open squares) corresponds to the intensity measured in the same scan, but at an exit angle of $\phi_f = 0°$, that is, at the horizon of the guide. (**B**) Measured (open circles) and simulated intensity (solid line) reflected in the vertical direction at $\alpha_i = \alpha_f$ as a function of α_i and at constant $\phi_i = 0.019°$ (first-order excitation in the *x* direction). The cusps in the top curves (1:2 scans) are accompanied by peaks in the bottom curves [1:1 scans (square symbols)]. Thus, a similar scenario as known from 1D waveguides occurs in both (orthogonal) directions. The 1:2 scans have been fitted by the standard Parratt algorithm to determine the parameters of the fabricated waveguide nanostructure. a.u., arbitrary units.

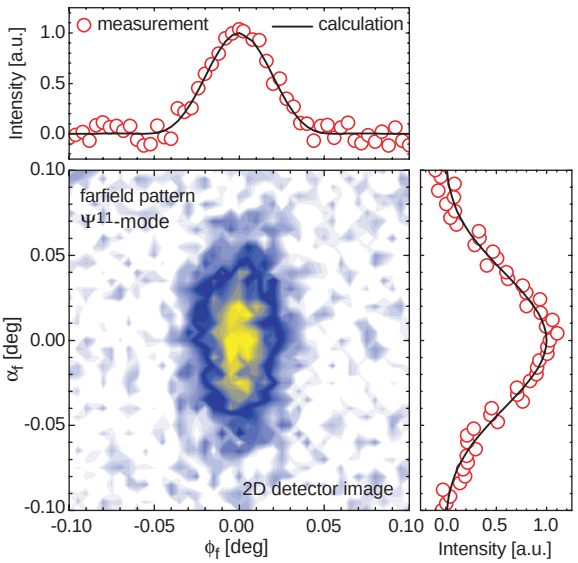

Fig. 4. Measured far-field diffraction pattern of the Ψ^{11} mode as a function of the two orthogonal exit angles ϕ_f and α_f (*x* and *z* directions on the 2D detector). On the top and at the right side of the 2D intensity plot, the integrated cross sections of the intensity distribution are shown as a function of ϕ_f and α_f, respectively, along with the simulated far-field pattern. The observed widths of the far-field pattern in both directions agree with the values expected for the Ψ^{11} mode.

References and Notes

1. D. H. Bilderback, S. A. Hoffman, D. J. Thiel, *Science* **263**, 201 (1994).
2. C. Riekel, *Rep. Prog. Phys.* **63**, 233 (2000) and references therein.
3. M. Sutton *et al.*, *Nature* **352**, 608 (1991).
4. D. Weiss, M. Peuker, G. Schneider, *Appl. Phys. Lett.* **72**, 1805 (1998).
5. Y. Suzuki *et al.*, *J. Synchrotron Radiat.* **4**, 60 (1997).
6. Y. P. Feng *et al.*, *Phys. Rev. Lett.* **71**, 537 (1993).
7. F. Pfeiffer *et al.*, *Proc. SPIE* **4145**, 193 (2001).
8. S. Lagomarsino *et al.*, *Appl. Phys. Lett.* **71**, 2557 (1997).
9. S. Di Fonza *et al.*, *Nature* **403**, 638 (2000).
10. F. Pfeiffer, U. Mennicke, T. Salditt, *J. Appl. Crystallogr.* **35**, 163 (2002).
11. M. J. Zwanenburg *et al.*, *Phys. Rev. Lett.* **85**, 5154 (2000).
12. For x-rays, δ and β are given by $\delta = \lambda^2 r_e n_e/2\pi$ and $\beta = \mu\lambda/(4\pi)$, where λ is the wavelength of the x-rays, r_e is the classical electron radius, n_e is the electron density, and μ is the absorption coefficient.
13. Because the aspect ratio between the length of the waveguide (several millimeters) and the width and height (several nanometers) is very large, we may assume the waveguide to be infinite in the *y* direction. Thus, the set of Maxwell equations reduces to the scalar wave equation, as shown in Eq. 1.
14. D. Marcuse, *Theory of Dielectric Optical Waveguides* (Academic Press, New York, 1974).
15. The solution of TE modes (polarization along the *x* axis) corresponds to the experiment, because the synchrotron radiation is highly polarized in the plane of the storage ring. However, the differences of TE and transverse magnetic modes (or, more generally, polarization effects) are very weak in the case of hard x-rays at grazing incidence angles.
16. The absorption has not been considered in our simulation, because β is very small for hard x-rays.
17. The following values were used: $n_1 = 0.999998436$ (PMMA), $n_2 = 0.999992183$ (Cr), $h = 62.2$ nm, $w = 140.3$ nm, and $\lambda = 0.097$ nm (*16*, *18*).
18. The geometric values *w* and *h*, as well as the density values of the core and the cladding (and, correspond-

ingly, the indices of refraction), were obtained from least squares fitting of the reflectivity (*29*) [see the vertical and horizontal 1:2 (reflectivity) scans in Fig. 3].
19. $k_{y,intern}$ is given by $k^2 = n^2(2\pi/\lambda)^2 = k_{x,intern}^2 + k_{y,intern}^2 + k_{z,intern}^2$, where $k_{x,intern} = nk\ \sin(\phi_{i,intern})$ and $k_{z,intern} = nk\ \sin(\alpha_{i,intern})$.
20. A. K. Ghatak, K. Thyagarajan, *Introduction to Fiber Optics* (Cambridge Univ. Press, Cambridge, 1998).
21. This case corresponds to the radiation modes or leaky modes of a waveguide and will not be discussed here (*14*, *19*).
22. The cutoff angle is obtained from $\alpha_{c,intern} = (\alpha_{c,cladding}^2 - \alpha_{c,core}^2)^{1/2}$, with a critical angle of $\alpha_c = (2\delta)^{1/2}$. With the above values, an internal cutoff angle of $\alpha_{c,internal} = 0.203°$ is obtained. Therefore, the guide supports seven resonance orders in the *x* direction (ϕ_{intern}) and three resonance orders in the *z* direction (α_{intern}).
23. The FWHM of the Ψ^{11} field intensity distribution in the waveguides guiding channel is 68.7 nm in the *x* direction and 33.0 nm in the *z* direction.
24. Photons can exit the guide at the end (rear face) if the footprint of the beam is separated from the end no farther than the so-called coupling length (in our case, ~750 μm).
25. Materials and methods are available as supporting material on *Science* Online.
26. The results shown here were obtained at the ID13 and ID01 beamlines (at the European Synchrotron Radiation Facility), with slightly different wavelengths but at comparable beam dimension and beam characteristics. In order to compare the results, the additional data set was rescaled to match the wavelength $\lambda = 0.097$ nm of the main experiment.
27. Standard reflectivity from thin-film layers is carried out by measuring the reflected intensity as a function of the angle on incidence, at $\alpha_i = \alpha_f$ and $\phi_i = \phi_f = 0$.
28. This nonstandard type of reflectivity, described in detail elsewhere, uses the fact that single, line-like nanostructures give rise to a circular diffraction pattern, subject to the constraint $q_y = 0$ ($\alpha_i^2 + \phi_i^2 = \alpha_f^2 + \phi_f^2$). Thus, by measuring the reflectivity in ϕ_i and ϕ_f at a fixed, small offset in α_i/α_f ($\alpha_i = \alpha_f \cong 0.05°$ was used in the present case), the lateral geometry (in the *x* direction) of the nanostructure can be probed. Values for the width *w* could thus be determined for several devices (a representative measurement and the corresponding fit are shown in Fig. 3A). Importantly, this circular diffraction pattern centered around the axis of the capillary observed for all angles may not be confused with the resonance effects.
29. L. G. Parratt, *Phys. Rev.* **95**, 359 (1954).
30. The mapping in Fig. 2D was obtained by modifying the refraction-corrected solution, displayed in Fig. 2B, according to the following equation:

$$I(\phi_i,\alpha_i) = \sum_{p,q} \exp\left(\frac{(\phi_i - \phi_i^p)^2}{2\sigma_{\phi i}^2}\right) \exp\left(\frac{(\alpha_i - \alpha_i^p)^2}{2\sigma_{\alpha i}^2}\right) \exp\left(\frac{(\phi_i^2 + \alpha_i^2) - ((\sigma_i^{p2}) + (\alpha_i^q))^2}{2\sigma_{radial}^2}\right) \quad (3)$$

with $\sigma_{\phi i} = 0.015°$, $\sigma_{\alpha i} = 0.01°$, and $\sigma_{radial} = 0.0011°$.
31. The rms roughness σ must not be small with respect to λ but with respect to λ/(sin α). In practice, total reflection can still occur up to about $\sigma \cong 1.5$ nm.
32. The measurements (not shown here) were carried out by scanning a 5-μm Ir/Pt pinhole (SPI, West Chester, PA) along the *x* and *z* directions on a piezo stage (Piezosystem Jena, Jena, Germany) at a distance of ≅1.0 mm behind the guide, confirming the exit beam divergence and thus also the conclusion that the exit beam originates from the end of the guide (waveguide point source).
33. This number exceeds the flux through a hypothetical pinhole of equivalent size by a factor of about 70. Improved fabrication can be expected to increase the output flux and hence the gain by orders of magnitude, similar to the recent progress in planar waveguides.

34. We thank H. Metzger for providing the additional time at beamline ID1 necessary to complement the ID13 data, as well as D. Le Belloc'h and A. Mazuelas for help at ID1. We are indebted to J. Kotthaus, H. Gaub, and J. Peisl at the Center for NanoScience Munich for advice and encouragement to carry out this project. We gratefully acknowledge financial support by Deutsche Forschungsgemeinschaft SFB-486.

Supporting Online Material
www.sciencemag.org/cgi/content/full/297/5579/230/DC1
Materials and Methods
Fig. S1
Table S1

19 March 2002; accepted 31 May 2002

Spin-Polarized Resonant Tunneling in Magnetic Tunnel Junctions

S. Yuasa,* T. Nagahama, Y. Suzuki

Insertion of a thin nonmagnetic copper Cu(001) layer between the tunnel barrier and the ferromagnetic electrode of a magnetic tunnel junction is shown to result in the oscillation of the tunnel magnetoresistance as a function of the Cu layer thickness. The effect is interpreted in terms of the formation of spin-polarized resonant tunneling. The amplitude of the oscillation is so large that even the sign of the tunnel magnetoresistance alternates. The oscillation period depends on the applied bias voltage, reflecting the energy band structure of Cu. The results are encouraging for the development of spin-dependent resonant tunneling devices.

A new field of electronics called spin electronics (*1, 2*), which makes use of both the electric charge and the spin of conduction electrons, has been developing rapidly in systems such as metallic magnetic multilayers, magnetic semiconductors, and strongly correlated electron systems. Among these systems, a magnetic tunnel junction (MTJ), which consists of two ferromagnetic (FM) metal layers (electrodes) separated by a thin insulating layer (tunnel barrier) and shows the tunnel magnetoresistance (TMR) effect (*3–5*), is especially important for application to magnetoresistive random-access memory (MRAM) devices. Highly functional spin-electronic devices such as spin transistors cannot be realized without a better understanding of the mechanism of spin-polarized electron transport, because it is still unclear how the coherence of the wave functions and spins of the conduction electrons are conserved in the transport process. For example, the resonant-tunneling effect (i.e., coherent tunneling of electrons from one electrode to the other through quantum well states formed between the two electrodes) (*6*), in which the coherence of electron wave functions is essential, has never been well controlled in spin-polarized systems such as MTJs and magnetic semiconductors. Spin-polarized resonant tunneling is crucial for the development of highly functional devices, such as a resonant-tunneling spin transistor (*7*) and quantum information devices, because the coherency of both the wave functions and the spins of conduction electrons should be conserved in those devices.

One of the simplest ways to realize spin-polarized resonant tunneling is to insert a nonmagnetic (NM) metal layer between the insulating tunnel barrier (I) and one of the two FM electrodes in a MTJ. Because spin-dependent reflections of the conduction electrons take place at the FM-NM interface (Fig. 1A), spin-polarized quantum well (QW) states are created in the NM layer (*8, 9*) and spin-polarized tunneling electrons will resonantly pass through the NM layer. Theories predict an oscillation of the TMR effect as a function of the NM layer thickness because the spin polarization of the tunneling electrons oscillates as a result of the resonant tunneling (*10, 11*). Although a number of experimental studies have been made, there have been no reports of an oscillation being observed (*12–17*). To date, the TMR ratio has usually been found to decrease monotonically with NM layer thickness (*12*). Moodera *et al*., using a NM Au layer (polycrystalline), first observed a sign reversal of the TMR ratio (*13*). Although it was attributed to a quantum size effect, no oscillation of the TMR was observed. LeClair used a NM Ru layer and obtained a similar result (*17*). The sign reversal of TMR was, however, attributed to a change of the density of states (DOS) of the electrode due to the interfacial mixing, not due to the quantum size effect. It was also found that the TMR effect almost disappears at a NM layer thickness of about 6 Å (*13–17*), indicating that the

NanoElectronics Research Institute, National Institute of Advanced Industrial Science and Technology, Tsukuba 305-8568, Japan, and Core Research for Evolutional Science and Technology, Japan Science and Technology Corporation, 4-1-8 Honcho, Kawaguchi 332-0012, Japan.

*To whom correspondence should be addressed. E-mail: yuasa-s@aist.go.jp